Linnera, Jarno; Karttunen, Antti J.

# Lattice dynamical properties of antiferromagnetic MnO, CoO, and NiO, and the lattice thermal conductivity of NiO

*Published in:*
Physical Review B

*DOI:*
10.1103/PhysRevB.100.144307

Published: 21/10/2019

*Document Version*
Publisher's PDF, also known as Version of record

# Lattice dynamical properties of antiferromagnetic MnO, CoO, and NiO, and the lattice thermal conductivity of NiO

Jarno Linnera and Antti J. Karttunen*

*Department of Chemistry and Materials Science, Aalto University, P.O. Box 16100, FI-00076 Aalto, Finland*

(Received 22 July 2019; revised manuscript received 1 October 2019; published 21 October 2019)

Lattice dynamical properties of antiferromagnetic rocksalt oxides are often interpreted using the cubic space group $Fm\bar{3}m$, although below Néel temperature their magnetic substructure possesses a lower symmetry. For example, in the case of NiO, a rhombohedral structural distortion lowers the symmetry to trigonal space group $R\bar{3}m$ below 525 K. We performed hybrid density functional theory calculations on the phonon dispersion relations of MnO, CoO, and NiO, and the lattice thermal conductivity of NiO using both $Fm\bar{3}m$ and $R\bar{3}m$ space groups. The calculated acoustic phonon frequencies of all oxides agree well with the available experimental data, while the optical modes of MnO and CoO show somewhat larger discrepancies. Our calculations show the phonon density of states to be very similar with both studied space groups. The experimental thermal conductivity of antiferromagnetic NiO is reproduced well below the Néel temperature by solving the linearized phonon Boltzmann transport equation.

DOI: 10.1103/PhysRevB.100.144307

## I. INTRODUCTION

The ability to conduct heat, that is, thermal conductivity, is a fundamental property of all matter. As such, it plays a vital role in the choice of material for many technological applications. For example, in microelectronics it is often desirable to maximize the thermal conductivity of some constituent material to ensure the removal of excess heat. In contrast, in thermoelectric applications the device efficiency is typically improved when the material conducts as little heat as possible. Still, despite the conceptually simple nature of the thermal conductivity, predicting it for a given material accurately with *ab initio* electronic structure methods is a relatively complex task [1,2]. In solids, heat is carried almost exclusively by electrons and phonons (lattice vibrations) and the total thermal conductivity $\kappa$ can be written as the sum of electronic and phononic contributions: $\kappa = \kappa_e + \kappa_l$. If the mobility of electrons in the material is low, like in insulators and undoped semiconductors, the contribution of electrons to heat transport can be neglected and it is enough to investigate only the lattice thermal conductivity.

The most used approach in computational thermal conductivity studies based on electronic structure methods is solving the linearized phonon Boltzmann transport equation (LBTE) [3–7]. In the most simplified form of LBTE, the so-called relaxation time approximation (RTA), the lattice thermal conductivity $\kappa_l$ can be expressed as the sum of the heat carried by the vibrational modes $\lambda$: $\kappa_l = 1/(NV_0)\sum_\lambda C_\lambda \mathbf{v}_\lambda \otimes \mathbf{v}_\lambda \tau_\lambda$, where $N$ is the number of $\mathbf{q}$ points sampled, $V_0$ is the volume of the unit cell, and $C_\lambda$, $\mathbf{v}_\lambda$, and $\tau_\lambda$ are the heat capacity, group velocity, and the relaxation time of the mode $\lambda$ (the norm of the product $\mathbf{v}_\lambda \tau_\lambda$ is called the mean free path of the mode). The most challenging component to evaluate, both from the point of view of computational time and accuracy, is the relaxation time $\tau_\lambda$. The evaluation of $\tau_\lambda$ requires the scattering rate matrix elements, which in turn require the third-order interatomic force constants (IFCs). The number of third-order IFCs scales immensely with system size, but the increase in computational power and methodological improvements have enabled the calculation of third-order IFCs with modern density functional theory (DFT) methods in reasonable timescales. As is common in quantum chemical calculations, space group symmetry can also be exploited to drastically reduce the computational time.

In addition to reducing computational cost, consideration of space group symmetry is also important in obtaining physically meaningful results for crystalline materials. As an example, the antiferromagnetic metal oxides MnO, CoO, and NiO are typically described in terms of cubic rocksalt structure ($Fm\bar{3}m$), but below their respective Néel temperatures of 116, 291, and 525 K, the symmetry is actually lower. The symmetry lowering is due to their magnetic substructure with antiferromagnetic ordering. Figure 1 illustrates the antiferromagnetic ordering, where parallel spin sheets in the [111] direction induce a small rhombohedral distortion [8]. Taking the symmetry lowering into account, spin-polarized computational studies should be carried out in the trigonal $R\bar{3}m$ subgroup with two metal atoms in the primitive cell. In contrast, the primitive cell of the $Fm\bar{3}m$ structure contains only one metal atom, preventing the use of antiferromagnetic ordering. The structural distortion due to magnetic ordering is, however, so small that in experiments the cubic space group is typically used to analyze for example phonon dispersion data obtained with inelastic neutron scattering [9–13].

One possibility to make the computational results obtained using the trigonal $R\bar{3}m$ subgroup comparable to the experimental results reported in the space group $Fm\bar{3}m$ is to use the so-called unfolding techniques, in which the force constants obtained using the two times larger trigonal primitive cell are

*antti.j.karttunen@iki.fi

 

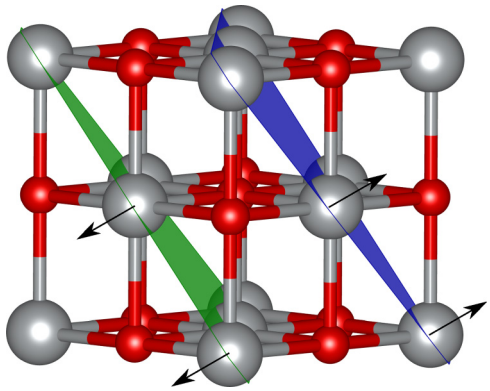

FIG. 1. Unit cell of an antiferromagnetic rocksalt oxide such as NiO ($Fm\bar{3}m$, gray: metal, red: oxygen). The colored planes are perpendicular to the [111] direction. Metal atoms on the green plane have the same spin while the atoms on the blue plane have the opposite spin, as indicated by the arrows.

folded back to the cubic primitive cell. The unfolding methods include projecting the phonon polarization vectors to a group of plane waves and calculating their appropriate unfolding weights, or averaging the force constants of the lower symmetry system to represent the higher symmetry system. There are few codes such as Phonon Unfolding and YPHON that serve this purpose for harmonic phonon properties [14,15]. However, such unfolding methods are not generally available for the third-order force constants that are required for the calculation of lattice thermal conductivity.

The phonon properties of magnetic materials are an active field of experimental research. The effect of an external magnetic field on the lattice thermal conductivity has been demonstrated recently and the possibility to control heat transport with magnetism is an attractive target [16]. *Ab initio* lattice thermal conductivity studies of magnetic materials using phonon Boltzmann transport are almost nonexistent, but the phonons, magnons, and lattice thermal transport of antiferromagnetic semiconductor MnTe have been recently investigated within the DFT+$U$ framework and BTE [17]. We are not aware of previous studies using hybrid DFT methods for the lattice thermal conductivity studies of magnetic $d$-metal oxides. It has been shown before that the use of hybrid DFT methods can improve the description of lattice dynamical properties of $d$-metal oxides [18]. The same effect can be achieved with a lower computational cost using GGA+$U$ approach, but hybrid DFT methods such as DFT-PBE0 have the advantage of not needing an additional material-dependent parameter.

We examine the lattice dynamical properties of antiferromagnetic MnO, CoO, and NiO, and the lattice thermal conductivity of NiO using hybrid DFT in conjunction with local Gaussian-type orbital (GTO) basis sets. We perform calculations using both the cubic ($Fm\bar{3}m$) and trigonal ($R\bar{3}m$) primitive cells to study the effects of the symmetry reduction due to antiferromagnetic ordering. In the case of the cubic primitive cell, we investigate the effect of neglecting the magnetic structure in the phonon calculations, treating the crystal as an effective alloy of spin-up and spin-down atoms analogously to the virtual crystal approximation [19]. This lowers the computational cost of the phonon calculations and enables the study of lattice dynamical properties with the higher cubic symmetry typically used in the experimental lattice dynamical studies of antiferromagnetic rocksalt oxides [9–13].

## II. COMPUTATIONAL DETAILS

Initial lattice parameters of MnO, NiO, and CoO were taken from the experimentally determined crystal structures by Sasaki *et al.* [20]. If one neglects the antiferromagnetic spin ordering and uses the cubic ($Fm\bar{3}m$) primitive cell with only one metal atom, DFT-PBE0 predicts the ground state to be metallic. As a result, all calculated properties would be inherently unphysical. The trigonal ($R\bar{3}m$) primitive cell for describing the antiferromagnetic ordering of the spins is obtained by forming new primitive lattice vectors $\mathbf{a}'$, $\mathbf{b}'$, and $\mathbf{c}'$ from the lattice vectors $\mathbf{a}$, $\mathbf{b}$, and $\mathbf{c}$ of the original face centered cubic primitive cell as follows: $\mathbf{a}' = \mathbf{b} + \mathbf{c}$, $\mathbf{b}' = \mathbf{a} + \mathbf{c}$ and $\mathbf{c}' = \mathbf{a} + \mathbf{b}$.

Geometry optimization in the trigonal space group $R\bar{3}m$ breaks the original cubic symmetry of the rocksalt structure and when the optimized trigonal structure is transformed back to cubic, the angles between the lattice vectors deviate slightly from 90°. The resulting angles in the optimized antiferromagnetic structures of MnO, CoO, and NiO are 90.7°, 90.2°, and 90.1°, respectively. The observed deviations from ideal cubic angle agree well with the respective experimental measurements of 90.7°, 89.6°, and 90.1°, although the deviation in CoO is in the opposite direction [21–23]. All lattice dynamical calculations within the cubic space group $Fm\bar{3}m$ were carried out for structures optimized within the trigonal space group $R\bar{3}m$, by setting the angle in the ideal value of 90°.

All DFT calculations were carried out with the CRYSTAL17 software package using the hybrid PBE0 exchange-correlation functional [24–26]. This includes calculations for geometry optimizations, band structures, static dielectric tensors [27–29], Γ-point vibrational frequencies [30,31], and forces in phonon supercells with atomic displacements. We employed a triple-$\zeta$-valence + polarization (TZVP) level Gaussian-type basis set in all calculations. The basis sets used for Ni and O have been described in a previous publication [32]. Co and Mn basis sets are described in the Supplemental Material [33]. Coulomb and exchange integral tolerance factors (TOLINTEG) were set to tight values of 8, 8, 8, 8, and 16.

In the geometry optimizations and Γ-point frequency calculations we used an $8 \times 8 \times 8$ **k** sampling for the reciprocal space [34]. We calculated the static dielectric tensors and Born effective charges in the trigonal $R\bar{3}m$ space group using the CPHF module of CRYSTAL17. The obtained trigonal static dielectric tensor elements and Born effective charges ($xx = yy \neq zz$) were made compatible with cubic symmetry ($xx = yy = zz$) by averaging. Differences in the trigonal static dielectric tensor elements $xx$ and $zz$ are rather small: $xx = 4.16$ and $zz = 4.15$ for MnO; $xx = 4.59$ and $zz = 4.63$ for NiO; $xx = 4.41$ and $zz = 4.42$ for CoO. The differences in the trigonal Born effective charges are slightly larger with $xx = 2.40$ and $zz = 2.27$ for MnO; $xx = 2.14$ and $zz = 2.19$ for NiO; $xx = 2.16$ and $zz = 2.30$ for CoO.

Harmonic and anharmonic phonon properties were investigated using the PHONOPY and PHONO3PY program packages, respectively [7,35]. In lattice dynamical calculations based on the frozen phonon method, the supercells with atomic displacements enable the use of correct magnetic ordering even in supercells generated from a cubic $Fm\bar{3}m$ primitive cell. The forces for the supercells are calculated in the $P1$ space group, which makes it possible to freely set the spins to the correct antiferromagnetic order, that is, to set antiparallel spins to the nickel atoms in adjacent (111) planes. The force constants and the dynamical matrix are constructed from the calculated forces assuming cubic symmetry, so that the correct magnetic ground state is implicitly included in the final phonon dispersions and lattice thermal conductivities even though it is not present in the $Fm\bar{3}m$ primitive cell.

In the force calculations for supercells with displacements, we applied tight SCF convergence criterion of $10^{-10}$ a.u. (TOLDEE). In the trigonal case, the second-order force constants were calculated using a $4 \times 4 \times 4$ supercell containing 256 atoms. In the the cubic case, a $6 \times 6 \times 6$ supercell containing 432 atoms was used. In both cases, only the $\Gamma$ point was considered in the $\mathbf{k}$ sampling. For the cubic MnO and NiO, we used the PHONOPY defaults of one displacement of 0.01 Å per atom. For CoO, we had to use two displacements of $\pm 0.06$ Å to obtain accurate force constants and to avoid imaginary phonon modes. The numerical difficulties in the case of CoO may be a result of the magnetic structure of CoO deviating towards a monoclinic $C2/m$ structure rather than the trigonal $R\bar{3}m$ [23]. The nonanalytical contribution as $\mathbf{q} \to 0$ has been taken into account in all phonon calculations. Phonon density of states were calculated using a $60 \times 60 \times 60$ $\mathbf{q}$ mesh for the trigonal primitive cell and an $80 \times 80 \times 80$ $\mathbf{q}$ mesh for the cubic primitive cell.

In the trigonal case, third-order force constants were calculated using a $2 \times 2 \times 2$ supercell, corresponding to 32 atoms ($4 \times 4 \times 4$ $\mathbf{k}$ sampling). For the cubic case, we used a $4 \times 4 \times 4$ supercell with 128 atoms ($2 \times 2 \times 2$ $\mathbf{k}$ sampling). For the third-order force constants, we used a pair-cutoff distance of 5 Å in the cubic case, meaning that all supercells where the displaced atoms were more than 5 Å apart were neglected. The cutoff was based on the lattice thermal conductivities obtained for the trigonal case using different cutoff values (see the Supplemental Material [33]). The phonon lifetimes were calculated using a $30 \times 30 \times 30$ $\mathbf{q}$ mesh for the cubic primitive cell and $20 \times 20 \times 20$ $\mathbf{q}$ mesh for the trigonal primitive cell. The convergence of the calculated lattice thermal conductivity with respect to $\mathbf{q}$ mesh is shown for the trigonal primitive cell in the Supplemental Material [33]. The isotope scattering due to the mass variance of natural isotope distributions was taken into account in all lattice thermal conductivity calculations as implemented in PHONO3PY.

In addition to RTA, we checked the effect of solving the full linearized Boltzmann transport equation (LBTE) for phonons when calculating the lattice thermal conductivity. The difference in $\kappa_l$ calculated at 300 K using the two methods was minimal: with trigonal primitive cell, both the full solution and RTA yield 24.7 W m$^{-1}$ K$^{-1}$ and with the cubic primitive cell, the values are 25.2 and 25.3 W m$^{-1}$ K$^{-1}$ with the full solution and RTA, respectively. At temperatures below 200 K, the relaxation-time approximation results in a slightly smaller $\kappa_l$ compared to LBTE. Using the trigonal primitive cell as an example, at 100 K RTA predicts $\kappa_l$ to be 140 W m$^{-1}$ K$^{-1}$, while the LBTE prediction is 148 W m$^{-1}$ K$^{-1}$ (5% increase). Further comparisons between RTA and LBTE at lower temperatures are shown in the Supplemental Material [33].

TABLE I. Optimized lattice parameters ($a$ and $c$ in Å), diagonals of the Born effective charges ($\mathbf{Z}^*$), and static dielectric tensors ($\epsilon_\infty$) of the studied oxides under the trigonal and cubic symmetries. In the trigonal system $a = b \neq c$ and $xx = yy \neq zz$, while in the cubic system $a = b = c$ and $xx = yy = zz$. For better readability, the tensor elements $xx$ and $zz$ are marked under $a$ and $c$, respectively. Experimental lattice parameters are from Sasaki *et al.* and static dielectric tensors from Plendl *et al.* [20,41].

| | NiO | | CoO | | MnO | |
|---|---|---|---|---|---|---|
| Trigonal ($R\bar{3}m$) | $a$ | $c$ | $a$ | $c$ | $a$ | $c$ |
| Lattice parameter | 2.96 | 14.48 | 3.02 | 14.71 | 3.16 | 15.19 |
| $\mathbf{Z}^*$ | 2.14 | 2.19 | 2.16 | 2.30 | 2.40 | 2.27 |
| $\epsilon_\infty$ | 4.59 | 4.63 | 4.41 | 4.42 | 4.16 | 4.15 |
| Cubic ($Fm\bar{3}m$) | $a$ | Expt. | $a$ | Expt. | $a$ | Expt. |
| Lattice parameter | 4.18 | 4.18 | 4.26 | 4.26 | 4.44 | 4.45 |
| $\mathbf{Z}^*$ | 2.16 | | 2.21 | | 2.35 | |
| $\epsilon_\infty$ | 4.60 | 5.7 | 4.41 | 5.3 | 4.16 | 4.95 |

## III. RESULTS

### A. Structural and electronic properties

Table I contains the optimized lattice parameters as well as the diagonals of the Born effective charge and high-frequency static dielectric tensors. In all three oxides, the changes in the cubic lattice parameter $a$ are minimal in comparison to the experiment. The magnetic moments of the metal atoms are 4.78, 2.72, and 1.67 $\mu_B$ for MnO, CoO, and NiO, respectively. The high-frequency static dielectric tensors are clearly underestimated with the used methods. The trend is correct, however, with NiO having the highest value, followed by CoO and MnO. The predicted band gaps for MnO, CoO, and NiO are 3.9, 3.9, and 5.3 eV, respectively. As is expected when using a hybrid functional, the predicted band gaps are larger in comparison to the experimental band gaps, which lie around 3.6 eV for MnO, 2.6 eV for CoO, and 4.0–4.3 eV for NiO [36–40]. As we focus here on the lattice dynamical properties, the electronic band structures and densities of states can be found from the Supplemental Material [33].

### B. Phonon dispersions

We calculated the phonon dispersions for MnO, CoO, and NiO both with cubic ($Fm\bar{3}m$) and trigonal ($R\bar{3}m$) primitive cells. Figure 2 shows the phonon dispersions obtained using the cubic primitive cell. The phonon dispersions of the three oxides show rather similar overall shape, especially for the acoustic phonons, but the phonon frequencies show differences. The agreement with experiment is generally very good for the acoustic modes, optical modes showing some larger differences.

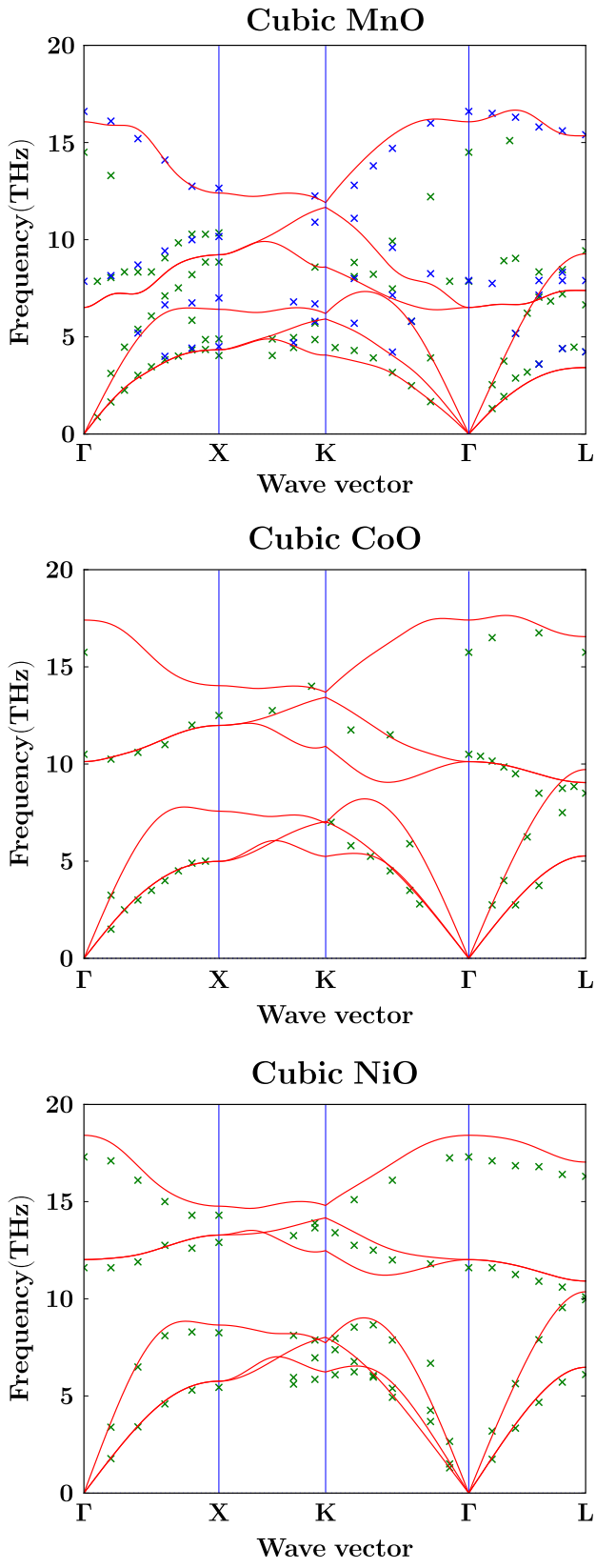


FIG. 2. Phonon dispersions of MnO, CoO, and NiO obtained using cubic primitive cells. In the case of MnO, blue crosses are experimental data points from Wagner *et al.* and green crosses from Haywood *et al.* For CoO and NiO, the green crosses correspond to experimental data from Sakurai *et al.* and Reichardt *et al.*, respectively [9–13].

For MnO, the experimental phonon dispersion data of Haywood *et al.* (green crosses) and Wagner *et al.* (blue crosses), are in reasonable overall agreement, but differ in the Γ-*X* direction for the LA mode and throughout the Brillouin zone for the LO mode [10,12,13]. The newer results of Wagner *et al.* are in better agreement with our DFT calculations. Our results are very close to the results of Wdowik *et al.*, who used GGA+$U$ with Hubbard parameter $U = 1$ eV [42]. The TO frequencies calculated here are underestimated in comparison to both experimental data sets. When Wdowik *et al.* increased $U$ all the way up to 7.9 eV, they found agreement with the experimental TO modes, as the corresponding force constants increased up to 50% with increasing $U$. Agreement for the LO mode did not improve, as the frequency at Γ is governed more by the terms in the nonanalytic term correction. It should be pointed out, however, that they compared only against the experimental frequencies of Haywood *et al.* and not the more recent data of Wagner *et al.* The discrepancies between the experiments show the need for definitive MnO phonon dispersion data that would enable more systematic improvement of the theoretical methodology. Additionally, the validity of using the cubic symmetry in interpreting the experimental results has been challenged in some studies, but the lack of experimental data for the lower trigonal symmetry has prevented developments in this direction [43,44].

The calculated phonon frequencies of CoO have good correspondence with the experiments in the Γ-*X* and Γ-*K* directions, and the agreement in the Γ-*L* direction is also reasonable. The optical modes in the Γ-*L* direction and the frequency of the LO mode at the Γ point show the largest differences in comparison to the experimental data. Wdowik *et al.* have studied CoO using the GGA+$U$ method with the cubic symmetry ($a = 4.27$ Å) and a refined $U$ value of 7.1 eV. Compared to our results, they obtained similar correspondence with the experiments in the Γ-*X* and Γ-*L* directions and even better agreement in Γ-*K* direction. The difference we have in the frequency of the LO mode at Γ appears to arise from the dielectric tensor and Born effective charge values used in the nonanalytical correction. If we use the same values as Wdowik *et al.* ($\epsilon_\infty = 5.3$, $\mathbf{Z}^* = 2.06$), our LO frequency matches exactly that of theirs and the experiments and the agreement for the first data point in the Γ-*L* direction is improved, too.

The bottom plot in Fig. 2 shows the phonon dispersions of NiO using the cubic symmetry. The rhombohedral distortion is the smallest for NiO and the cubic symmetry yields a good agreement with the experimental data points from inelastic neutron scattering by Reichardt *et al.* [11]. The acoustic phonons and the TO modes are well reproduced by our calculations. The only clear discrepancies modes are seen for the acoustic modes in few points in the Γ-*K* direction and for the highest-energy LO mode. Generally, the shape of LO band follows the experimental data points well, but the calculated frequencies are somewhat overestimated in comparison to the experimental data, similar to CoO.

Figure 3 shows the phonon dispersions and phonon density of states (DOS) calculated for NiO with both cubic and trigonal primitive cells. Our phonon dispersions calculated with the trigonal primitive cell are mostly in good agreement with the previous phonon dispersions calculated by Floris

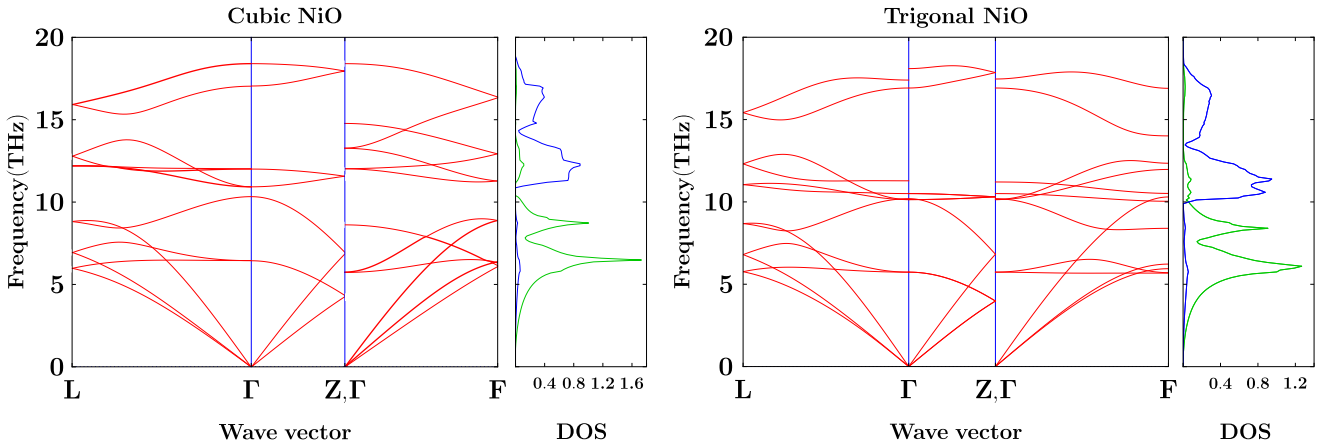


FIG. 3. Phonon dispersions and atom-projected phonon density of states (DOS) of NiO using two different primitive cells. The phonon dispersions of the cubic primitive cell were plotted in directions corresponding to the trigonal primitive cell, folded, and labeled according to the trigonal case. The following reciprocal space points were used for the cubic primitive cell: $L = (-1/2, 1/2, 1/2)$, $Z = (1/2, 1/2, 1/2)$, and $F = (-1/2, 1/2, 0)$. Corresponding points for the trigonal primitive cell are: $L = (0, 1/2, 0)$, $Z = (1/2, 1/2, 1/2)$, and $F = (1/2, 1/2, 0)$. In the DOS plots the green and blue lines correspond to Ni and O contributions, respectively.

*et al.* using PBE+$U$ approach [45]. The work of Floris *et al.* also highlights well the major differences between the phonon dispersions obtained with pure PBE and PBE+$U$. The acoustic modes obtained with PBE0 and PBE+$U$ possess similar frequencies, but some of PBE0 optical modes are found at higher frequencies compared to PBE+$U$. For example, the highest optical mode at the zone edge $F$ is 1.2 THz higher for PBE0. The largest differences are seen in a few optical modes in the direction Γ-$F$ where the modes show larger dispersion with the PBE+$U$ approach. The phonon DOS obtained with PBE0 shows somewhat sharper features in comparison to PBE+$U$, but the overall distributions are in line with each other.

Although the cubic and trigonal primitive cells correspond to different Brillouin zones, it is possible to compare the phonon dispersions between the primitive cells. This is accomplished by considering the smaller cubic primitive cell as a segment of the larger trigonal primitive cell, plotting the phonon dispersions in the equivalent directions, and folding them. As a result, the phonon dispersions of the cubic primitive cell are labeled with the labels of the trigonal primitive cell in Fig. 3. A somewhat similar comparison of theoretical phonon dispersions of NiO was done by Aytan *et al.*, who found that lifting the band degeneracy with larger primitive cells produces a better match between the calculated Γ-point frequencies and measured Raman spectra [46]. In the directions Γ-$L$ and Γ-$Z$, there is a straightforward mapping between the two primitive cells and the folded phonon dispersions of the cubic primitive cell are well in line with the phonon dispersions of the trigonal primitive cell. The most obvious difference is that the cubic primitive cell shows a clear gap between the acoustic and optical modes right above 10 THz, while there is no such gap in the trigonal primitive cell. In the Γ-$Z$ direction, the optical phonon modes of the two primitive cells also show differences. The direction Γ-$F$ is a lower symmetry direction in the trigonal primitive cell, as illustrated by the lifting of the band degeneracies at the $F$ point. In this direction, the folded phonon dispersions of the cubic primitive cell show larger differences with the trigonal primitive cell compared to the two other directions.

The phonon DOS plots of the cubic and the trigonal primitive cells can be compared directly and they are clearly similar. The shape of the DOS of optical modes above 10 THz is somewhat different, and the optical DOS peak is at a slightly higher frequency in the cubic primitive cell, but the general distribution is the same for the two primitive cells. As expected, the lower frequency modes below 10 THz are mainly due to the motion of the heavier nickel atoms and the higher frequency modes result from the motion of the oxygen atoms. The phonon DOS plot of the trigonal primitive cell with composition $Ni_2O_2$ has actually two overlapping green and blue lines, which explains why the $x$-axis range of the phonon DOS is similar for the cubic and trigonal primitive cell. When integrating the phonon DOS over the frequency range, the trigonal case has twice the number of phonon modes in comparison to the cubic case.

For MnO and CoO, the phonon DOS obtained with the cubic and trigonal primitive cell show slightly more pronounced differences compared to NiO. Since we focus on NiO in the lattice thermal conductivity calculations, the cubic and trigonal phonon DOS of MnO and CoO can be found from the Supplemental Material [33].

### C. Lattice thermal conductivity

The BTE approach used here for calculating the lattice thermal conductivity does not take into account any changes in the magnetic structure induced by higher temperatures. The temperature only affects the populations of the phonon states. Because of this, we present and discuss lattice thermal conductivity here only for NiO, where the Néel temperature is high enough (525 K) to ensure that the antiferromagnetic ground state we use corresponds to the magnetic configuration during the experimental lattice thermal conductivity measurements and we do not enter regions of magnetic behavior that our approach cannot describe. It is worth mentioning that more intricate models capable of including

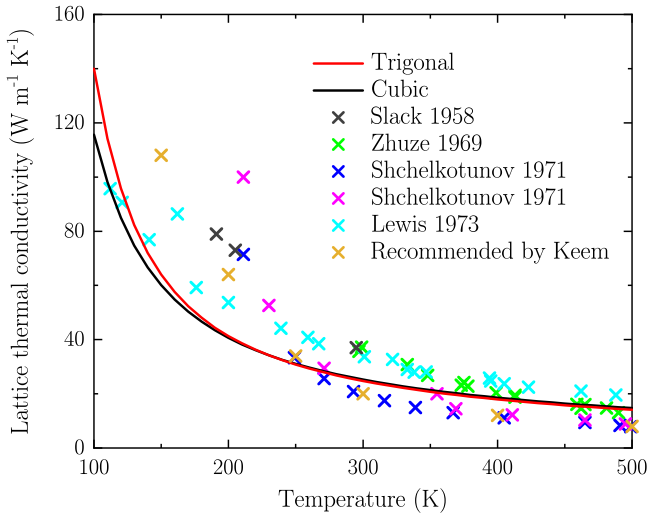


FIG. 4. Lattice thermal conductivity of NiO calculated using both the trigonal (red line) and cubic (black line) primitive cells. Crosses denote the different experimental data points [48–52].

magnon-phonon interactions are being developed, see, e.g., the paper of Mikhail *et al.* and references therein [47].

In line with the matching phonon DOS obtained from the cubic and trigonal primitive cells, the predicted lattice thermal conductivities are also practically equal (Fig. 4). The agreement between the experimental $\kappa$ and calculated $\kappa_l$ is generally very good. The experimental data in Fig. 4 have been obtained from the review of Keem and Honig and were chosen from experiments that are consistent with each other and have been obtained from good quality single crystals [48–52]. Interestingly, the results of the two samples of Shchelkotunov *et al.* form a somewhat unified line, whereas the results of Zhuze *et al.* and Lewis *et al.* correspond better with one another. Below 250 K, the values recommended by Keem are between those of Shchelkotunov and Lewis and follow Shchelkotunov at higher temperatures. The data from Slack are closer to Shchelkotunov at lower temperatures but at 300 K they agree with Zhuze and Lewis. Our theoretical results are in good agreement with the experiments of Lewis at lower temperatures, but lower than Keem's recommended values. Above 250 K the trend changes and our calculations yield $\kappa_l$ values that are higher than than Keem's recommended values.

The fact that our predicted lattice thermal conductivity is smaller than the experimental thermal conductivity below 250 K is a rather unusual feature. One would expect the opposite, as the calculations entirely neglect some scattering pathways which would reduce $\kappa_l$. These include, e.g., the scattering resulting from magnon-phonon interactions, point defects, and boundaries. As discussed in the Computational Details, using denser **q** meshes or the full solution of the linearized Boltzmann transport equation does not change the situation, although the full solution slightly improves the agreement with experiment at temperatures below 200 K. The reason behind the low-temperature discrepancy between theory and experiment is unknown at this point and requires further studies. From a methodological point of view, the use

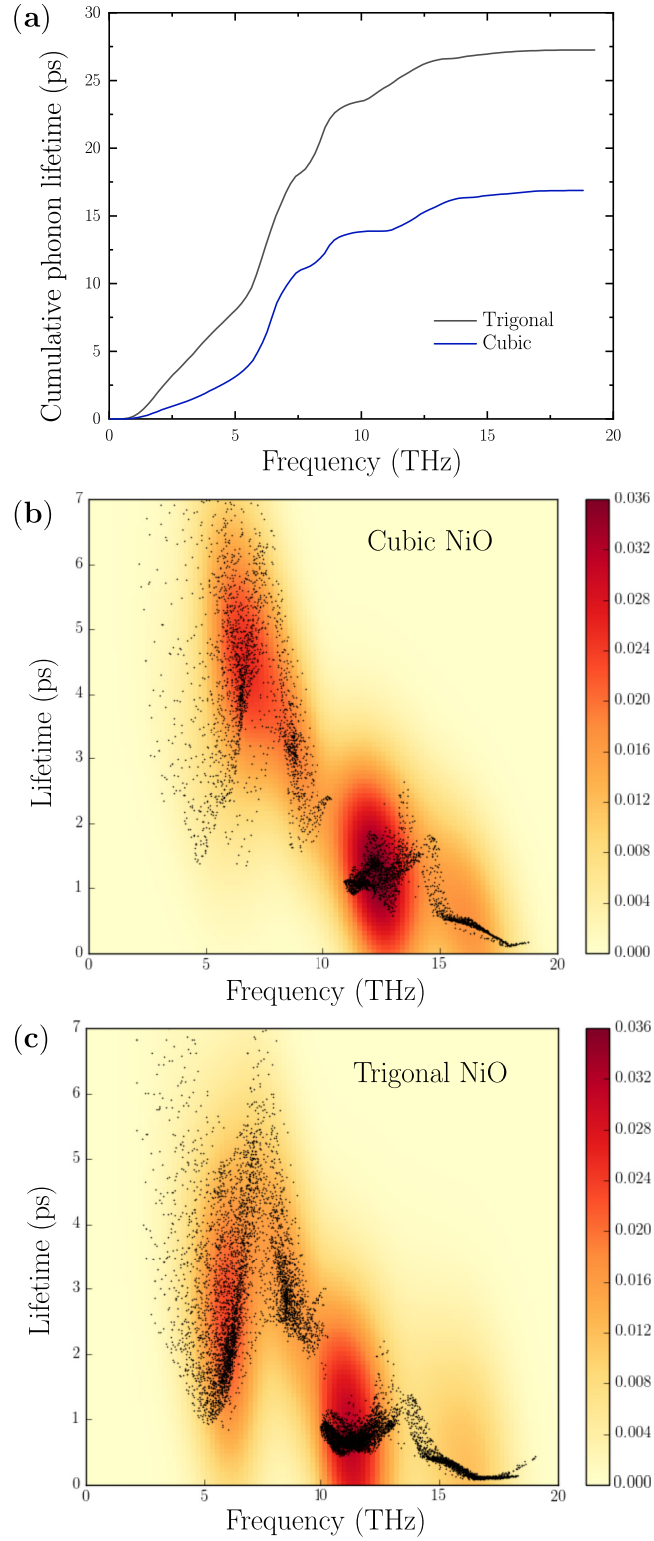


FIG. 5. Phonon lifetimes of NiO at 300 K calculated using the cubic and trigonal primitive cells. (a) Cumulative phonon lifetimes for both primitive cells. (b) and (c) Phonon lifetimes plotted on top of the phonon density of states for the cubic and trigonal primitive cells, respectively. Color map on the right is for the density of points on the lifetime-frequency plane. The $y$ axis has been cut in such way that only the highest-density region in the frequency-lifetime plane is shown. Plots with full $y$ axis and phonon lifetimes up to 250 ps are shown in the Supplemental Material [33].

of noncollinear spin formalism would be an improvement, but we do not expect this to play a major role in the case of NiO.

The three factors that contribute to the lattice thermal conductivity of a phonon mode, namely the heat capacities, group velocities, and phonon lifetimes, are very similar for both cubic and trigonal primitive cells. A convenient way of examining the phonon properties is to plot them cumulatively over the whole frequency range of the phonon dispersion. Figure 5(a) shows the cumulative phonon lifetime for both cubic and trigonal primitive cells at 300 K. At 300 K, the predicted $\kappa_l$ is 24.7 W m$^{-1}$ K$^{-1}$ for the trigonal primitive cell and 25.3W m$^{-1}$ K$^{-1}$ for the cubic primitive cell. The cumulative phonon group velocities and heat capacity are presented in the Supplemental Material [33].

As the phonon lifetimes are calculated based on the possible decay and scattering pathways that obey energy and momentum conservation laws [7], similar phonon DOS produces a similar shape for the cumulative phonon lifetimes, even though the shape of the Brillouin zone is different for the two different primitive cells. The absolute value of the cumulative phonon lifetime for the trigonal primitive cell is roughly twice that of the cubic primitive cell in Fig. 5. This is expected, as the trigonal primitive cell has twice as many atoms and phonon group velocity and heat capacity show similar behavior. The final lattice thermal conductivities are normalized by the volume of the primitive cell ($V_0$). The small differences in the phonon DOS just above 10 THz give rise to small differences in cumulative phonon lifetimes, as the cubic primitive cell shows a small plateau, but the trigonal primitive cell does not.

Figures 5(b) and 5(c) show the calculated phonon lifetimes plotted against the phonon frequency, with a heat map representing the density of the lifetime distribution at 300 K. To some extent, this also depicts the regular phonon DOS, but with the additional information of the phonon lifetimes at given frequencies. The distributions of lifetimes between cubic and trigonal primitive cells are qualitatively alike, owing much to the similar phonon DOS. The plateau in Fig. 5(a) for the cubic primitive cell at about 10 THz can be seen as an empty space without any data points in Fig. 5(b), whereas in Fig. 5(c) there are points continuously throughout the whole frequency range. The gap around 10 THz in the trigonal case contains only a few points in between the denser zones. Without any information from the cubic primitive cell, it would be much more difficult to deduce this point as the jump from acoustic to optical phonon modes. Additionally, accurately interpreting the amount of heat carried by acoustic and optical phonons would be difficult from the trigonal primitive alone, as there are more modes in the unit cell, and the optical modes extend down to around 5 THz while in the cubic system they appear only above 10 THz. These plots also hint towards the intuitive conclusion that more phonon modes result in more collision and decay pathways, leading to shorter lifetimes. Looking at the heat map, the highest density of $\tau_\lambda$ is between 4 and 5 ps for the acoustic modes of the cubic primitive cell, but the highest density point falls between 2 and 4 ps in the trigonal primitive cell.

## IV. CONCLUSIONS

We employed hybrid density functional theory to investigate the lattice dynamical properties of antiferromagnetic rocksalt oxides MnO, CoO, and NiO, and the lattice thermal conductivity of NiO. The antiferromagnetic order was incorporated in the phonon calculations in two different ways, using cubic ($Fm\bar{3}m$) and trigonal ($R\bar{3}m$) primitive cells. Incorporating the antiferromagnetic order in the phonon supercell calculations enabled us to interpret the phonon properties for a cubic primitive cell with only one metal atom which is not large enough to describe the antiferromagnetic ground state as such. Comparison of the phonon dispersions and phonon properties shows that the results from the cubic and trigonal primitive cells agree well. The predicted phonon dispersion relations are in line with experimental data, the agreement being the best for NiO, where the rhombohedral distortion is the smallest and more recent experimental data is available. In the case of NiO, the cubic and trigonal primitive cells lead in practically identical lattice thermal conductivities, which also agree with the experimental measurements. In other words, it is possible to investigate the lattice thermal conductivity of magnetic materials with the original nonmagnetic primitive cell if the the symmetry breaking due to magnetic ordering is relatively small and the magnetic ordering is incorporated in the phonon supercell calculations.

## ACKNOWLEDGMENTS

The work has been funded by the Academy of Finland (Strategic Research Council, CloseLoop consortium, Grants No. 303452 and No. 317273). Computational resources were provided by CSC, the Finnish IT Center for Science.

[1] L. Lindsay, C. Hua, X. Ruan, and S. Lee, Survey of *ab initio* phonon thermal transport, Mater. Today Phys. **7**, 106 (2018).

[2] G. Fugallo and L. Colombo, Calculating lattice thermal conductivity: A synopsis, Phys. Scr. **93**, 043002 (2018).

[3] T. Tadano, Y. Gohda, and S. Tsuneyuki, Anharmonic force constants extracted from first-principles molecular dynamics: applications to heat transfer simulations, J. Phys. Condens. Matter. **26**, 225402 (2014).

[4] J. Carrete, B. Vermeersch, A. Katre, A. van Roekeghem, T. Wang, G. K. Madsen, and N. Mingo, almaBTE : A solver of the space-time dependent Boltzmann transport equation for phonons in structured materials, Comput. Phys. Commun. **220**, 351 (2017).

[5] A. Chernatynskiy and S. R. Phillpot, Phonon transport simulator (PhonTS), Comput. Phys. Commun. **192**, 196 (2015).

[6] W. Li, J. Carrete, N. A. Katcho, and N. Mingo, ShengBTE: A solver of the Boltzmann transport equation for phonons, Comput. Phys. Commun. **185**, 1747 (2014).

[7] A. Togo, L. Chaput, and I. Tanaka, Distributions of phonon lifetimes in Brillouin zones, Phys. Rev. B **91**, 094306 (2015).

[8] C. Kittel, *Introduction to Solid State Physics* (Oxford University Press, Oxford, 2004).

[9] J. Sakurai, W. J. L. Buyers, R. A. Cowley, and G. Dolling, Crystal dynamics and magnetic excitations in cobaltous oxide, Phys. Rev. **167**, 510 (1968).
[10] V. Wagner, W. Reichard, and W. Kress, Lattice dynamics of MnO, in *Proc. Conf. Neutron Scattering* (Gatlinburg, USA, 1976), Vol. 1, p. 175.
[11] W. Reichardt, V. Wagner, and W. Kress, Lattice dynamics of NiO, J. Phys. C **8**, 3955 (1975).
[12] B. C. G. Haywood and M. F. Collins, Lattice dynamics of MnO, J. Phys. C **2**, 46 (1969).
[13] B. C. Haywood and M. F. Collins, Optical phonons in MnO, J. Phys. C **4**, 1299 (1971).
[14] F. Zheng and P. Zhang, Phonon Unfolding: A program for unfolding phonon dispersions of materials, Comput. Phys. Commun. **210**, 139 (2017).
[15] Y. Wang, L.-Q. Chen, and Z.-K. Liu, YPHON: A package for calculating phonons of polar materials, Comput. Phys. Commun. **185**, 2950 (2014).
[16] H. Jin, O. D. Restrepo, N. Antolin, S. R. Boona, W. Windl, R. C. Myers, and J. P. Heremans, Phonon-induced diamagnetic force and its effect on the lattice thermal conductivity, Nat. Mater. **14**, 601 (2015).
[17] S. Mu, R. P. Hermann, S. Gorsse, H. Zhao, M. E. Manley, R. S. Fishman, and L. Lindsay, Phonons, magnons, and lattice thermal transport in antiferromagnetic semiconductor MnTe, Phys. Rev. Mater. **3**, 025403 (2019).
[18] J. Linnera and A. J. Karttunen, *Ab initio* study of the lattice thermal conductivity of $Cu_2O$ using the generalized gradient approximation and hybrid density functional methods, Phys. Rev. B **96**, 014304 (2017).
[19] L. Bellaiche and D. Vanderbilt, Virtual crystal approximation revisited: Application to dielectric and piezoelectric properties of perovskites, Phys. Rev. B **61**, 7877 (2000).
[20] S. Sasaki, K. Fujino, and Y. Takéuchi, X-ray determination of electron-density distributions in oxides, MgO, MnO, CoO, and NiO, and atomic scattering factors of their constituent atoms, P. Jpn. Acad. B-Phys. **55**, 43 (1979).
[21] A. K. Cheetham and D. A. O. Hope, Magnetic ordering and exchange effects in the antiferromagnetic solid solutions $Mn_xNi_{1-x}O$, Phys. Rev. B **27**, 6964 (1983).
[22] S. Saito, K. Nakahigashi, and Y. Shimomura, X-ray diffraction study on CoO, J. Phys. Soc. Jpn. **21**, 850 (1966).
[23] W. Jauch, M. Reehuis, H. J. Bleif, F. Kubanek, and P. Pattison, Crystallographic symmetry and magnetic structure of CoO, Phys. Rev. B **64**, 052102 (2001).
[24] R. Dovesi, A. Erba, R. Orlando, C. M. Zicovich-Wilson, B. Civalleri, L. Maschio, M. Rérat, S. Casassa, J. Baima, S. Salustro, and B. Kirtman, Quantum-mechanical condensed matter simulations with CRYSTAL, Wires Comput. Mol. Sci. **8**, e1360 (2018).
[25] J. P. Perdew, K. Burke, and M. Ernzerhof, Generalized Gradient Approximation Made Simple, Phys. Rev. Lett. **77**, 3865 (1996).
[26] C. Adamo and V. Barone, Toward reliable density functional methods without adjustable parameters: The PBE0 model, J. Chem. Phys. **110**, 6158 (1999).
[27] M. Ferrero, M. Rérat, R. Orlando, and R. Dovesi, The calculation of static polarizabilities of 1–3D periodic compounds. the implementation in the crystal code, J. Comput. Chem. **29**, 1450 (2008).
[28] M. Ferrero, M. Rérat, B. Kirtman, and R. Dovesi, Calculation of first and second static hyperpolarizabilities of one- to three-dimensional periodic compounds. Implementation in the CRYSTAL code, J. Chem. Phys. **129**, 244110 (2008).
[29] M. Ferrero, M. Rérat, R. Orlando, and R. Dovesi, Coupled perturbed Hartree-Fock for periodic systems: The role of symmetry and related computational aspects, J. Chem. Phys. **128**, 014110 (2008).
[30] F. Pascale, C. M. Zicovich-Wilson, F. López Gejo, B. Civalleri, R. Orlando, and R. Dovesi, The calculation of the vibrational frequencies of crystalline compounds and its implementation in the CRYSTAL code, J. Comput. Chem. **25**, 888 (2004).
[31] C. M. Zicovich-Wilson, F. Pascale, C. Roetti, V. R. Saunders, R. Orlando, and R. Dovesi, Calculation of the vibration frequencies of $\alpha$-quartz: The effect of Hamiltonian and basis set, J. Comput. Chem. **25**, 1873 (2004).
[32] J. Linnera, G. Sansone, L. Maschio, and A. J. Karttunen, Thermoelectric properties of p-type $Cu_2O$, CuO, and NiO from hybrid density functional theory, J. Phys. Chem. C **122**, 15180 (2018).
[33] See Supplemental Material at http://link.aps.org/supplemental/10.1103/PhysRevB.100.144307 which includes Refs. [53–56], electronic band structures, third-order force constant cut-off tests, phonon dispersions and phonon DOS plots for MnO and CoO, cumulative phonon group velocity and volumetric heat capacity of NiO, **q**-mesh convergence tests, isotope scattering tests, phonon lifetimes of NiO, the full solution of LBTE vs RTA at low temperatures, and the used GTO basis sets.
[34] H. J. Monkhorst and J. D. Pack, Special points for Brillouin-zone integrations, Phys. Rev. B **13**, 5188 (1976).
[35] A. Togo and I. Tanaka, First principles phonon calculations in materials science, Scr. Mater. **108**, 1 (2015).
[36] A. Fujimori and F. Minami, Valence-band photoemission and optical absorption in nickel compounds, Phys. Rev. B **30**, 957 (1984).
[37] S. Hüfner, J. Osterwalder, T. Riesterer, and F. Hulliger, Photoemission and inverse photoemission spectroscopy of NiO, Solid State Commun. **52**, 793 (1984).
[38] E. Z. Kurmaev, R. G. Wilks, A. Moewes, L. D. Finkelstein, S. N. Shamin, and J. Kuneš, Oxygen x-ray emission and absorption spectra as a probe of the electronic structure of strongly correlated oxides, Phys. Rev. B **77**, 165127 (2008).
[39] D. R. Huffman, R. L. Wild, and M. Shinmei, Optical absorption spectra of crystal-field transitions in MnO, J. Chem. Phys. **50**, 4092 (1969).
[40] H.-h. Chou and H. Y. Fan, Effect of antiferromagnetic transition on the optical-absorption edge in MnO, $\alpha$-MnS, and CoO, Phys. Rev. B **10**, 901 (1974).
[41] J. Plendl, L. Mansur, S. Mitra, and I. Chang, Restsrahlen spectrum of MnO, Solid State Commun. **7**, 109 (1969).
[42] U. D. Wdowik and D. Legut, *Ab initio* lattice dynamics of MnO, J. Phys. Condens. Matter. **21**, 275402 (2009).
[43] S. Massidda, M. Posternak, A. Baldereschi, and R. Resta, Noncubic Behavior of Antiferromagnetic Transition-Metal Monoxides with the Rocksalt Structure, Phys. Rev. Lett. **82**, 430 (1999).

[44] E. M. L. Chung, D. M. Paul, G. Balakrishnan, M. R. Lees, A. Ivanov, and M. Yethiraj, Role of electronic correlations on the phonon modes of MnO and NiO, Phys. Rev. B **68**, 140406(R) (2003).

[45] A. Floris, S. de Gironcoli, E. K. U. Gross, and M. Cococcioni, Vibrational properties of MnO and NiO from DFT+$U$-based density functional perturbation theory, Phys. Rev. B **84**, 161102(R) (2011).

[46] E. Aytan, B. Debnath, F. Kargar, Y. Barlas, M. M. Lacerda, J. X. Li, R. K. Lake, J. Shi, and A. A. Balandin, Spin-phonon coupling in antiferromagnetic nickel oxide, Appl. Phys. Lett. **111**, 252402 (2017).

[47] I. Mikhail, I. Ismail, and M. Ameen, Model calculation of thermal conductivity in antiferromagnets, Physica B (Amsterdam) **476**, 29 (2015).

[48] G. A. Slack and R. Newman, Thermal Conductivity of MnO and NiO, Phys. Rev. Lett. **1**, 359 (1958).

[49] V. P. Zhuze, O. N. Novruzov, and A. I. Shelykh, Thermal conductivity near a continuous-phase transition, Fiz. Tverd. Tela **11**, 1287 (1969) [Sov. Phys. – Solid State **11**, 1044 (1969)].

[50] V. A. Shchelkotunov and V. N. Danilov, Effect of magnetic state of ferrimagnetics and anti-ferromagnetics of basic structural type on mechanism of heat energy spreading, Izv. Akad. Nauk. SSSR, Ser. Fiz. **35**, 1158 (1971).

[51] F. B. Lewis and N. H. Saunders, The thermal conductivity of NiO and CoO at the Neel temperature, J. Phys. C **6**, 2525 (1973).

[52] J. E. Keem and J. M. Honig, Selected electrical and thermal properties of undoped nickel oxide, Purdue University, Indiana (1978), https://apps.dtic.mil/docs/citations/ADA128940.

[53] W. Setyawan and S. Curtarolo, High-throughput electronic band structure calculations: Challenges and tools, Comput. Mater. Sci. **49**, 299 (2010).

[54] K. N. Kudin and G. E. Scuseria, Linear-scaling density-functional theory with Gaussian orbitals and periodic boundary conditions: Efficient evaluation of energy and forces via the fast multipole method, Phys. Rev. B **61**, 16440 (2000).

[55] A. J. Karttunen, T. Tynell, and M. Karppinen, Atomic-level structural and electronic properties of hybrid inorganic-organic ZnO:hydroquinone superlattices fabricated by ALD/MLD, J. Phys. Chem. C **119**, 13105 (2015).

[56] F. Weigend and R. Ahlrichs, Balanced basis sets of split valence, triple zeta valence and quadruple zeta valence quality for H to Rn: Design and assessment of accuracy, Phys. Chem. Chem. Phys. **7**, 3297 (2005).